# Reinforcements in avian wing bones: Experiments, analysis, and modeling

E. Novitskaya[a,*], C.J. Ruestes[a,b], M.M. Porter[a,c], V.A. Lubarda[a,d], M.A. Meyers[a,d], J. McKittrick[a]

[a] *Department of Mechanical and Aerospace Engineering and Materials Science and Engineering Program, University of California, San Diego, 9500 Gilman Dr., La Jolla, CA 92093, USA*
[b] *Universidad Nacional de Cuyo, Facultad de Ciencias Exactas y Naturales and CONICET, M5502JMA, Mendoza, Argentina*
[c] *Department of Mechanical Engineering, Clemson University, Clemson, SC 29634, USA*
[d] *Department of NanoEngineering, University of California, 9500 Gilman Dr., La Jolla, CA 92093, USA*

## ARTICLE INFO

## ABSTRACT

Almost all species of modern birds are capable of flight; the mechanical competency of their wings and the rigidity of their skeletal system evolved to enable this outstanding feat. One of the most interesting examples of structural adaptation in birds is the internal structure of their wing bones. In flying birds, bones need to be sufficiently strong and stiff to withstand forces during takeoff, flight, and landing, with a minimum of weight. The cross-sectional morphology and presence of reinforcing structures (struts and ridges) found within bird wing bones vary from species to species, depending on how the wings are utilized. It is shown that both morphology and internal features increases the resistance to flexure and torsion with a minimum weight penalty. Prototypes of reinforcing struts fabricated by 3D printing were tested in diametral compression and torsion to validate the concept. In compression, the ovalization decreased through the insertion of struts, while they had no effect on torsional resistance. An elastic model of a circular ring reinforced by horizontal and vertical struts is developed to explain the compressive stiffening response of the ring caused by differently oriented struts.

## 1. Introduction

### 1.1. Bird wing skeletons and wing motion

Birds and flying mammals (bats) have lightweight skeletons, which coupled with a high lift to weight ratio, make flight possible. Birds range in mass from several grams (hummingbird) to more than 100 kg (ostrich), with overall range of birds weighing between 10 g and 10 kg (Silva et al., 1997). For bald eagles, the skeleton amounts to only 7% of the body mass, $\sim^1/_3$ of what the feathers represent (Brodkorb, 1955). For flight, other adaptations have evolved such as having a smaller number of bones compared to terrestrial vertebrates, and the fusion of some bones (Proctor and Lynch, 1993; Wolfson, 1955). Birds also have a complex pulmonary system; many have pneumatic bones (particularly the proximal limb bones - the humerus and femur) that are directly connected to the respiratory system, thereby increasing buoyancy (Proctor and Lynch, 1993; Gill, 2007; O'Connor and Claessens, 2005). Flying birds have more hollow bones (not marrow filled) than flightless birds (e.g. ostrich, penguin) (Proctor and Lynch, 1993). Diving birds and hummingbirds have few hollow bones. The diving birds need to have a higher density skeleton to propel themselves through water, and for hummingbirds, the weight savings involved with hollow bones is minimal (Proctor and Lynch, 1993). Bird bones are characterized by a much thinner sheath of cortical bone, compared to terrestrial animals (Currey and Alexander, 1985). The mean bending strength and flexural modulus were found to be significantly higher for marrow-filled than pneumatic bones, but these calculations do not incorporate the differences in moment of inertia due to the internal structure (Cubo and Casinos, 2000). The ratio of internal to external radius is larger in pneumatic bones ($\sim 0.80$) than in marrow filled bones ($\sim 0.65$), which results in a mass advantage of pneumatic over marrow filled bones, estimated to be between 8% and 13% by Pauwell (Pauwells, 1980) and Currey and Alexander (Currey and Alexander, 1985).

The bird wing skeleton consists of the humerus ('upper arm'), which is attached to the main flight muscles in the breast, the ulna and radius (radio-ulna or 'forearm'), carpometacarpus ('wrist' and 'hand') and the phalanges ('fingers'). These are shown in Fig. 1 for a turkey vulture (*Cathartes aura*) wing (Novitskaya et al., 2014). Turkey vultures comprise the largest group of New World vultures and are large, soaring birds with an average wingspan of $\sim 1.7$ m, weigh between 1–2 kg, and feed exclusively on carrion. During flight, the ulna (the main load-bearing element of the radio-ulna) is roughly perpendicular to the humerus, which itself is shorter and thicker, since it needs to withstand larger forces (Proctor and Lynch, 1993).
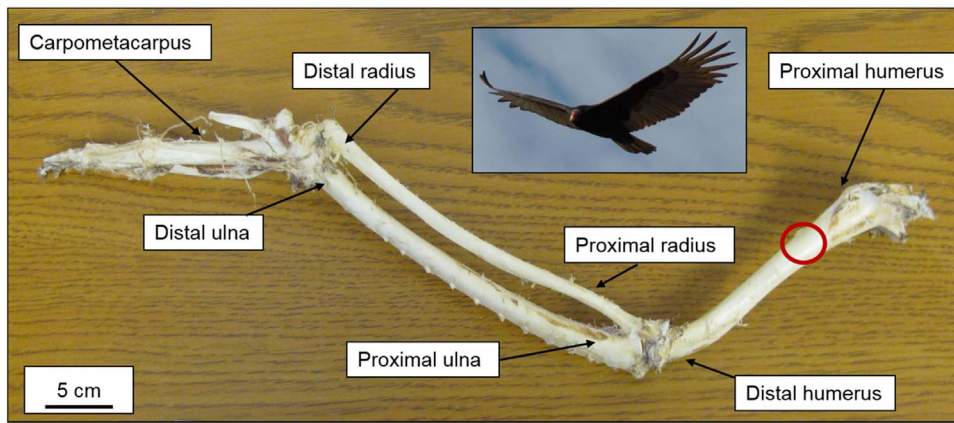
**Fig. 1.** Photograph of the bones in the left wing of a turkey vulture, pointing out the humerus (attached to the body), radius, ulna and carpometacarpus. Adapted from (Novitskaya et al., 2014). The red circle indicates the area of maximum bending and torsion moments during flight (Pennycuick, 2008). (For interpretation of the references to color in this figure legend, the reader is referred to the web version of this article.)

Wing motion can be classified as flapping/soaring (flapping wings and soaring, e.g. vultures, eagles), flapping/gliding (flapping wings and gliding, e.g. seagulls, pelicans), flapping (with periodic gliding, e.g. ravens, crows) and flightless (e.g. emus, ostriches and rheas) (Pennycuick, 2008; Bruderer et al., 2010). Microstructural analysis was recently performed on the cross-sections of humeri and ulnae for several flying and non-flying bird species (Novitskaya et al., 2014). It was found that thickness of the bone walls was not uniform for all flying birds due to presence of external pressure and stress distribution in them during the flight. Additionally, it was concluded that bones from flapping/soaring and flapping/gliding birds had ovalized sections, while bones from flapping and non-flying birds have more circular cross-sections.

### 1.2. Bird bone adaptations

An interesting example of structural adaptation in nature is the internal structure of avian wing bones, which consists of reinforcing structures (struts and ridges, see Fig. 2) (Proctor and Lynch, 1993; Pennycuick, 2008). The bones need to be sufficiently strong and stiff to withstand forces during takeoff, flight, and landing. Wing bones have to resist both bending and torsion loads; they are rarely loaded in pure tension or compression. Due to the high metabolic cost of creating bone, it is believed that the reinforcing structures in bird wing bones grow in response to specific stresses experienced by flying birds, and therefore should be optimal for their purpose. As with mammalian bone, there is a periosteal and endosteal sheath surrounding the cortical bone and a medullary core that is filled with less dense trabecular bone, as shown in the schematic illustration in Fig. 2b. Examples of struts commonly found in many avian bones are shown in Fig. 2a,c from a condor femur and turkey vulture humerus, respectively, for illustrative purposes. The struts are isolated rods that span across the interior diameter of the bone. The struts cannot be classified as trabecular bone because the density of the array is too low. They appear to be at locations "in need," working against extensive bending forces and preventing the localized buckling of bone walls. They are mainly found on the ventral side of the wing bones of flying birds (Novitskaya et al., 2014; Pennycuick, 2008). Interestingly, the ulnae of the vulture and gull (soaring and gliding birds) have the struts, while ulnae of the raven and duck (flapping and non-flying birds) lack those (Novitskaya et al., 2014). The ridges are rod-like in appearance that lay flat against the interior wall (Fig. 2d). The orientation of the ridges likely develops at about ± 45° to horizontal axis to help carry large tensile stresses developed during torsion along those directions. Maximum tensile and compressive stresses are generated at ± 45° to the longitudinal axis. Ridges aligned in these directions will decrease tensile stresses that occur in torsional loading and reverse torsional loading. Since failure in bone is produced by tensile stresses, the configuration of ridges along such directions is most effective (Fig. 2e).

Table 1 lists some of the physical and mechanical properties of humeri and ulnae for different birds, compared to bovine femur bone. The bird bones have higher porosity and lower density, compared to the bovine bone. Additionally, among the birds, the domestic duck has the highest porosity and lowest mineral content, indicating that having high wing bone strength is not essential for a non-flying birds. The present values for the density of the humerus are lower than the mean density found in perching birds (Dumont, 2010), which suggests that a reduction in mineral content for larger soaring and gliding birds is a beneficial development for weight savings and increasing toughness.

The current study will describe in details the influence of struts on the mechanical performance of bird wing bones, while the impact of ridges will be summarized in another publication. Particularly, we analyze the internal structure of wing bones from a turkey vulture and a California condor (*Gymnogyps californianus*) to assess the contribution of reinforcing struts to bending (ovalization) and torsion resistance. Additionally, bone prototypes with reinforcing structures (struts) were fabricated by 3D printing and mechanical testing was performed to investigate ovalization and torsional behaviors. Finally, an elastic model of a circular ring reinforced by horizontal and vertical struts was developed to explain the stiffening of the ring caused by the differently oriented struts.

## 2. Mechanics background

### 2.1. Bending and torsion analysis of thin walled sections

Fig. 3a shows the main torsion and bending axes and their respective moment arms for wing bones during activity. During lift, the dominant bending and torsion moment are balanced by a downward pull of the pectoralis muscle. From Fig. 3a one can see that the humerus is subjected to significant torsion. The "radio-ulna unit" can only rotate in the plane of the wing, and is subjected to a bending moment from the outer part of the wing. This is transmitted through the joint as a twisting moment on the humerus (Pennycuick, 1967). The bending and torsional moments carried by the humerus are transferred to the proximal end of the radio-ulna through the elbow joint. The points of application of the forces are marked in the feathers and are approximately 25% of their length. This is, of course, an approximation that integrates the distributed load on the feather due to the aerodynamic force. The bending moment and torsion axes for a specific feather with respect to the humerus are shown in Fig. 3a. The bending moment arm with respect to the proximal end of the humerus is $\overline{OB}$ and torsion arm is $\overline{OA}$. The bending moment is $M = F \times \overline{OB}$ and the torque is $T = F \times \overline{OA}$. The humerus has evolved to resist bending and torsion, and is has adapted to resist torsion at both microscopic and macrostructural levels (de Margerie et al., 2006).

For simplicity, the wing bones of flying birds can be considered as a hollow cylinder with thin walls. If placed in bending, the relationship
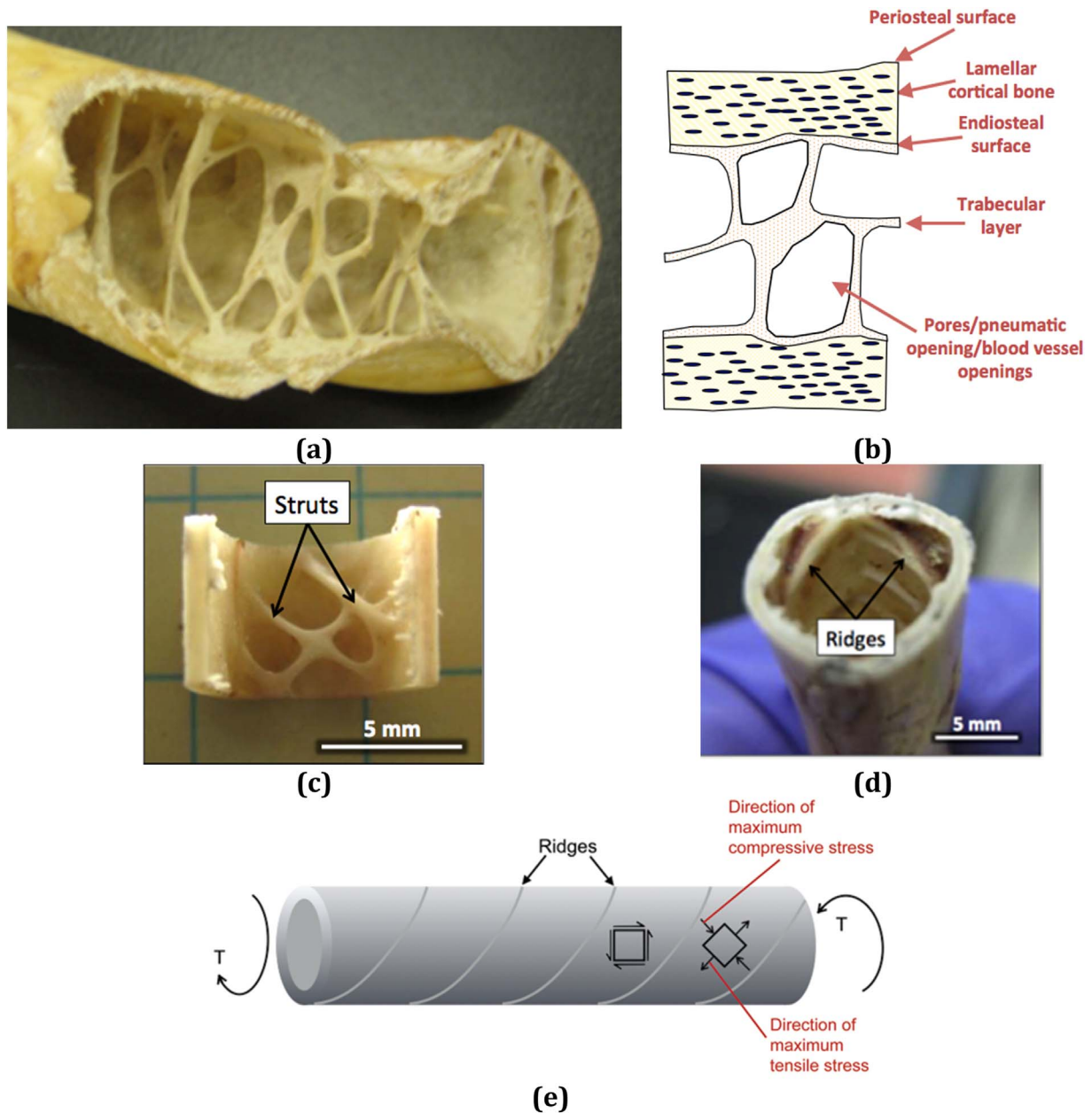
**Fig. 2.** Condor femur: **(a)** Photograph of the bone interior showing an array of struts that are isolated rods spanning across the interior diameter of the bone and **(b)** cross-sectional schematic diagram of the bone components in a wing, which is similar to the structure of mammalian bone, having a periosteal and endiosteal sheath surrounding the cortical bone and a medullary core that is filled with less dense bone. Adapted from (Davis, 1998). Turkey vulture humerus: **(c)** Longitudinal cross-section, showing an array of struts (truss-like), with the struts at ~ 45°. **(d)** Top view showing the ridges, which are rod-like in appearance and lay flat against the interior wall, either parallel to the diameter or slightly angled from the long axis of the bone. **(c)** and **(d)** taken from (Kiang, 2013). **(e)** Schematic diagram of how the orientation of the ridges may form in the interior of wing bones as a result of torsional forces (*T*): the oriented ridges resist torsional rotation because reinforcement ridges are aligned with the direction of maximum tensile stress, implying that the ridges increase resistance to tensile fracture.

**Table 1**
Mineral content, density, porosity and microhardness of the humerus (H) and ulna (U) in bird bones compared to bovine cortical femur bone (Novitskaya et al., 2014).

| | Mineral content (wt%) | | Density (g/cm³) | | Porosity (%) | | Microhardness (MPa) | |
|---|---|---|---|---|---|---|---|---|
| | H | U | H | U | H | U | H | U |
| **Turkey vulture** | 60 ± 1 | 61 ± 2 | 1.6 ± 0.1 | 1.2 ± 0.1 | 11 ± 2 | 11 ± 2 | 400 ± 100 | 400 ± 100 |
| **California gull** | 66 ± 1 | 65 ± 2 | 1.4 ± 0.1 | 1.3 ± 0.1 | 13 ± 3 | 9 ± 1 | 580 ± 50 | 510 ± 80 |
| **Common raven** | 64 ± 2 | 63 ± 1 | 1.3 ± 0.1 | 1.5 ± 0.1 | 14 ± 1 | 13 ± 3 | 560 ± 60 | 580 ± 50 |
| **Domestic duck** | 43 ± 1 | 43 ± 1 | 1.2 ± 0.2 | 1.3 ± 0.2 | 20 ± 4 | 20 ± 4 | 330 ± 40 | 310 ± 50 |
| **Bovine cortical femur bone** | 65 ± 2 (Novitskaya et al., 2011) | | 2.0 ± 0.2 (Novitskaya et al., 2011) | | 8 ± 1 (Novitskaya et al., 2011) | | 550–700 (Currey et al., 2001; Zioupos et al., 2000) | |

**(a)**



**(b)**
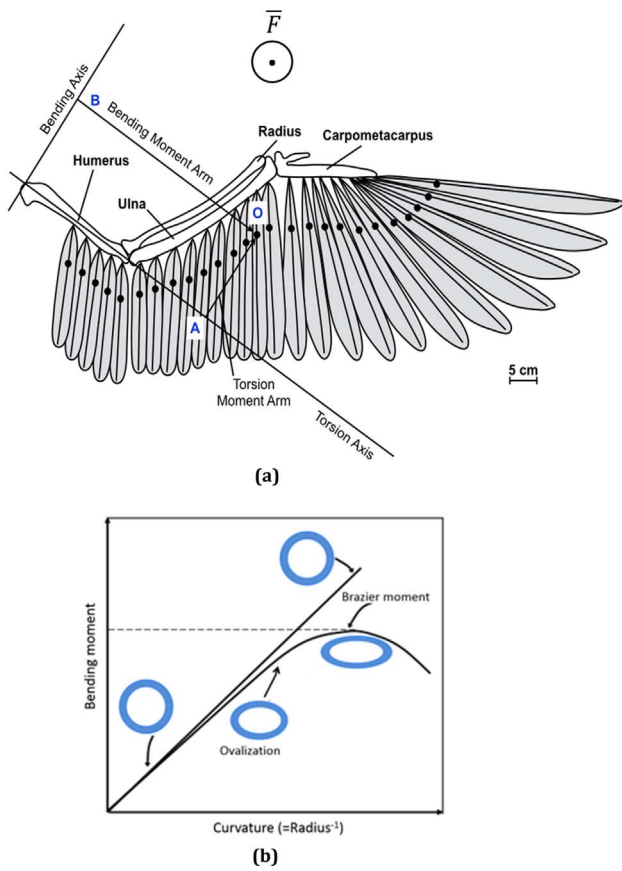
**Fig. 3. (a)** A gliding wing showing the bending and torsion axes and bending and torsion moment arms. The solid dots mark the centers of lift. The torsion arm is the distance between the center of lift and the neutral axis of torsion in the humerus. Lift applies a moment about the torsion axis of the humerus. A bending moment occurs in the radio-ulna that is transmitted through the joint to the humerus as a torsional moment at the distal end. The bending moment in the proximal end of humerus is $M = F \times \overline{OB}$ and the torsional moment is $T = F \times \overline{OA}$. **(b)** Bending moment as a function of the curvature ($\kappa =$ radius$^{-1}$) for two cylindrical tubes, one of a higher stiffness material (top straight line) and one of a lower stiffness material (lower curve). If the stiffness is not sufficient, ovalization of the cross section is more pronounced and the curve deviates from linearity. At a critical bending moment (dashed line), the tube undergoes buckling causing collapse (Brazier buckling). Adapted from (Pennycuick, 2008).

between the moment ($M$) and the curvature ($\kappa =$ radius$^{-1}$) experienced on the hollow cylinder can be determined by classical beam theory, $M = EI\kappa$, where $EI$ is the bending stiffness, $E$ being the modulus of elasticity and $I$ is the second moment of the cross-sectional area. For a thin circular tube of outer radius $R$ and wall thickness $t$, the second moment $I$ can be approximated by $I \sim \pi R^3 t$, and the maximum bending stress is then given by $\sigma = M/(\pi R^2 t)$. Similarly, the maximum shear stress due to applied torque $T$ is $\tau = T/(2\pi R^2 t)$. Both expressions indicate that increasing the wall thickness decreases both torsional and bending stresses, at the expense of an increase in weight, which is undesirable for a bird. Given that $I$ and $J$ (polar moment of inertia) are only a function of the geometry, these values have evolved (and increased) in birds to decrease in mass while ensuring that the stresses are within the elastic limit, thus improving the flight performance.

However, if the cross-section becomes too slender (internal/external diameter ratio approaching 1) a number of problems can occur. During bending the midsection can ovalize, if the material is not of sufficient stiffness, as shown in Fig. 3b. This figure compares the bending moment as a function of $\kappa$ for two tubes, one that has a higher stiffness and one with a lower stiffness. The higher stiffness material retains its circular shape as the moment increases and has a linear $M - \kappa$ relationship (straight line). If the stiffness is not sufficient, ovalization of the cross

section occurs and the curve deviates from linearity (curved line), because the second moment of the cross sectional area for the horizontal axis substantially decreases. At a critical bending moment, the ovalization is so pronounced that a hollow cylinder undergoes local buckling causing collapse. This is called Brazier buckling (Brazier, 1927), and typically occurs at ~50% of the stress of the tube that retains its circular cross-section. Thus, ovalization (with the major axis of the ellipse in the direction perpendicular to the applied load) needs to be minimized to avoid Brazier buckling during bending.

For a given bending moment, the maximum stress on the surface of a tube can be reduced if $I$ is increased. Fig. 4a-d illustrates circular and elliptical cross-sections with their respective second moments of area. With the major axis of the ellipse perpendicular to the applied load (Fig. 4c), the ratio of the second moments of area of an elliptical to a circular tube is:

$$\frac{I_x^{ellipse}}{I_x^{circle}} = \frac{\frac{\pi}{4} b^3 t \left(1 + \frac{3a}{b}\right)}{\pi R^3 t} = \frac{2\beta^2(3 + \beta)}{(1 + \beta)^3} \qquad (1)$$

where $a$ and $b$ are the major and minor semi-axes of the ellipse, $t$ is its average (constant) thickness and $\beta = b/a$ ($< 1$). With mass conserved, the cross-sectional areas for circular and elliptical tubes are the same, which implies $a = 2R/(1 + \beta)$. At the onset of ovalization, $\beta$ decreases from 1, and as it decreases further, $I_x$ for the ellipse becomes increasing smaller compared to the corresponding circular cross-section, as shown in Fig. 4e. This unwanted effect leading to Brazier buckling can be offset by increasing $I$:

(1) locally, by adding a material at the position of the maximum bending moment, or
(2) globally, the bone could remodel to form an ellipse where the major axis is parallel to the applied load (Fig. 4d).

For (1), the addition of material can take two forms: struts and ridges. The presence of struts and ridges decrease the maximum stress in the bone, and are also beneficial to the prevention of localized buckling of the bone. Importantly, struts can minimize ovalization by ensuring that the ratio $\beta = b/a$ does not change. They act as internal columns or tension elements.

For (2), it is known that bone remodels in response to mechanical loads (Ruff et al., 2006), the bone can form an ellipse with the major axis oriented parallel to the direction of the applied load (Fig. 4d), then the ratio of second moments of area is:

$$\frac{I_y^{ellipse}}{I_y^{circle}} = \frac{\frac{\pi}{4} a^3 t \left(1 + \frac{3b}{a}\right)}{\pi R^3 t} = \frac{2(1 + 3\beta)}{(1 + \beta)^3} \qquad (2)$$

This is graphically illustrated in Fig. 4e, showing that as ovalization progresses ($\beta$ decreasing), $I_y$ increases thereby decreasing the maximum stress on the bone. Ovalization with the major axis in the direction of the applied load also increases the Brazier buckling resistance by increasing the area moment of inertia.

The same type of analysis can be applied to torsional resistance. For a thin-walled hollow circular and elliptical cylinders, the torsional moment of inertia is:

$$J^{circle} = 2\pi R^3 t,$$

$$J^{ellipse} = \frac{4\pi^2 a^2 b^2 t}{L} \qquad (3)$$

where $L = 4aE(e)$ is the length of the midline of the elliptical cross-section (average perimeter), and $E(e)$ is the complete elliptical integral of the second kind, with $e = \sqrt{1-\beta^2}$. The ratio of the torsional moments of inertia for an elliptical hollow cross-section and the circular one is thus:
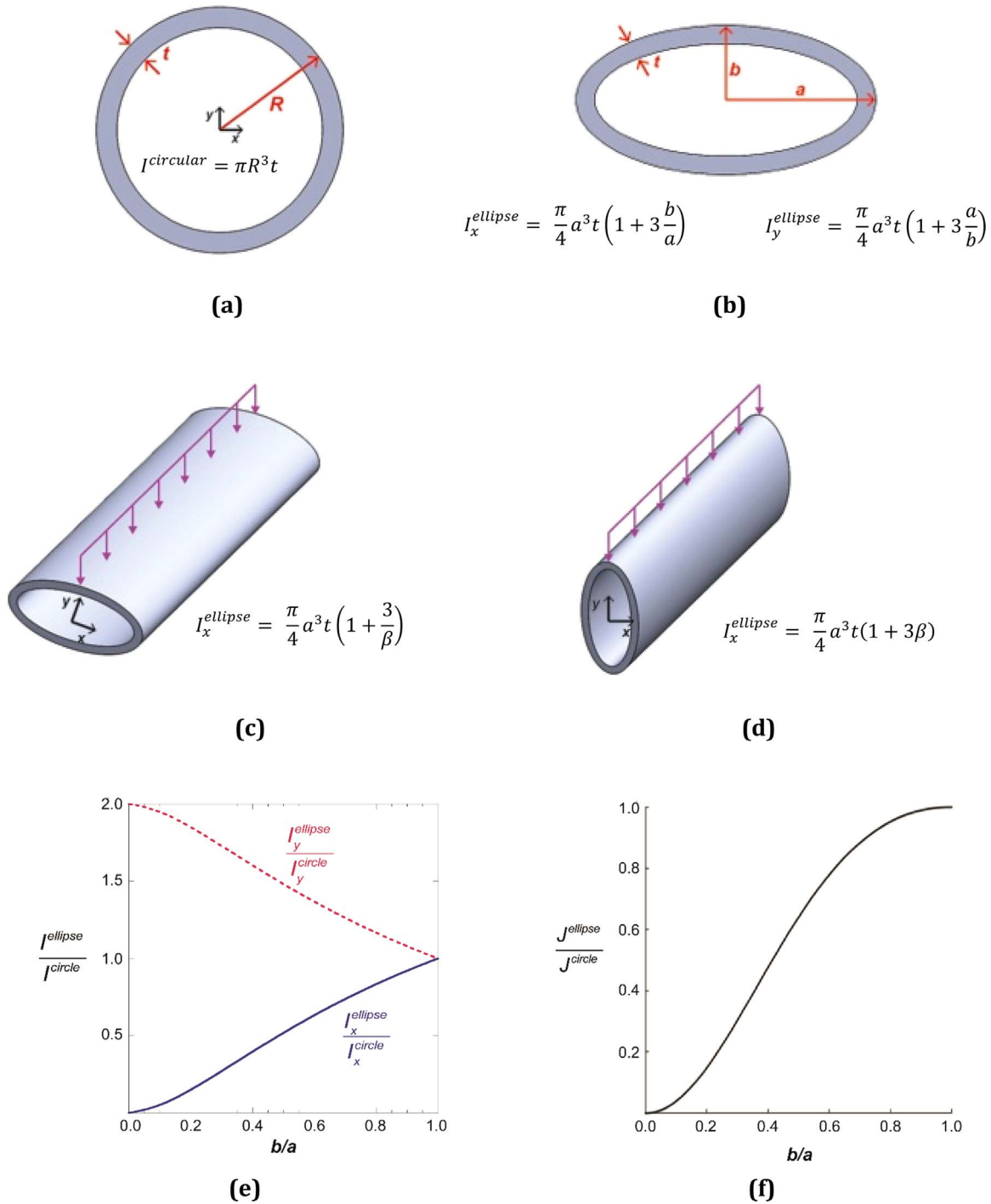
$$I^{circular} = \pi R^3 t$$

**(a)**

$$I_x^{ellipse} = \frac{\pi}{4} a^3 t \left(1 + 3\frac{b}{a}\right) \qquad I_y^{ellipse} = \frac{\pi}{4} a^3 t \left(1 + 3\frac{a}{b}\right)$$

**(b)**

$$I_x^{ellipse} = \frac{\pi}{4} a^3 t \left(1 + \frac{3}{\beta}\right)$$

**(c)**

$$I_x^{ellipse} = \frac{\pi}{4} a^3 t (1 + 3\beta)$$

**(d)**

**(e)**

**(f)**

**Fig. 4.** (a) A hollow cylinder with radius *R* and wall thickness *t* with the second moment of area. (b) A hollow ellipse having major axis *a* and minor axis *b* with constant thickness *t*. (c) If the load is applied in the direction of the minor axis, the second moment of area decreases over that of a circular cross-section. (d) If the load is applied in the direction of the major axis, the second moment of area increases over that of a circular cross-section. (e) Plot of the normalized second moments of area as a function of $b/a = \beta$ for the loading conditions in (c) – solid line and (d) – dashed line. (f) Plot of the polar moment of inertia for an ellipse normalized to that of a circular cross-section, showing that as ovalization increases, $J_{ellipse}$ decreases.

$$\frac{J^{ellipse}}{J^{circle}} = \frac{\frac{a^2 b^2 t}{\sqrt{(a^2 + b^2)/2}}}{R^3 t} = \frac{4\beta^2}{(1 + \beta^2)^2},$$

$$R = a\sqrt{(1 + \beta^2)/2} \tag{4}$$

The above expression is valid approximately in the range $1/3 < \beta < 3$, in which the perimeter of the ellipse can be determined from an approximation $L = 2\pi a\sqrt{(1+\beta^2)/2}$. The expression

$R = a\sqrt{(1+\beta^2)/2}$ follows from the condition of equal areas of the thin-walled circular and elliptical cross-sections ($2\pi Rt = Lt$), assuming that both sections have the same constant wall thickness, *t*.

Eq. (4) indicates that ovalization, i.e., the decrease of $\beta$, reduces the polar moment of inertia (Fig. 4f), thereby decreasing the torsional resistance and increasing the shear stress in the bone. This can be remedied by adding material locally (ridges). The presence of struts has far less effect on torsional resistance, since they can rotate almost freely during torsion.

## 2.2. Bend to twist ratio

Adaptations to bending or torsional resistance can be quantified by the 'bend-to-twist' ratio, *EI/GJ*, indicating that if this ratio is large, the beam more easily twists than bends and vice versa (Pennycuick, 2008; Pilkey, 2003; Lubarda, 2009; Etnier, 2003; Vogel, 1992). This ratio depends on materials properties (*E* and *G,* the respective elastic and shear moduli of the bone material) and shape factors (*I* and *J,* the respective area and polar moments of inertia of the bone geometry). The average values for *E* from a variety of birds were reported as 10.5 GPa for the humerus and 12.1 GPa for the ulna (Casinos and Cubo, 2001), which is roughly half that of mammalian skeletal bone (about 20 GPa (Novitskaya et al., 2011)). For turkey leg bones *G* was reported as 0.98 GPa (Spatz et al., 1996). The ratio *E/G* for bird bones (∼ 10) is larger than for an isotropic solid (∼ 3) or for cortical bovine femur bone (∼ 7) (Reilly and Burstein, 1975), indicating the shape factors are important elements that can give the beam more bending or torsional resistance. Biological materials that are slender columns (e.g. plant stems, long bones) can adapt their cross-sectional shape according to environmental forces (e.g. wind, movement forces) to maximize their bending and/or torsion resistance (Pennycuick, 2008; Niklas, 1992). Several researchers have reported on torsional and bending resistance of wing bones. In pigeons, the torsional and bending resistance were the same for the humerus, while the torsional resistance in the radio-ulna was greater than the bending resistance (Pennycuick, 1967). Strain gauges attached to live pigeons recorded considerable torsion, and dorsoventral bending was produced in the humerus (Biewerner and Dial, 1995). It was concluded that the critical design feature for this bone was torsion resistance. Torsional resistance during flight has been proposed to be more significant than bending resistance for bat wing bones (Swartz et al., 1992). In other work on 22 bird species, it was suggested that macro- and micro-structural features were developed in the humerus and ulna to enhance the torsion resistance, and in the radius and carpometacarpus to increase the bending resistance (de Margerie et al., 2006).

## 3. Materials and methods

Wing bone samples were gathered from a flapping/soaring bird, a turkey vulture, which was found dead in the Anza Borrego desert in California. Samples were stored in ambient dry condition at room temperature and normal humidity. Wing bones (humerus, ulna and carpus) from another vulture, the California condor, were provided by the San Diego Museum of Natural History. Those two birds were chosen due to their ultimate ability to soar which presumably is one of the most important factors in the formation of the reinforcing struts inside the wing bones.

### 3.1. Micro-computed tomography (μ-CT)

Wing bones (humerus, ulna and carpus) from the condor were scanned with a micro-computed tomography (μ-CT) scanner (Skyscan 1076, Kontich, Belgium) inside a dry plastic tube. The imaging was performed at 36 μm isotropic voxel sizes applying an electric potential of 70 kV and a current of 200 μA, using a 0.5 mm aluminum filter. Images and 3D rendered models were developed using Skyscan's DataViewer and CTVox software.

### 3.2. 3D printed sample preparation

3D prototypes of the bones with reinforcing struts were prepared using ABS (acrylonitrile-butadiene-styrene, with a density equal to 1.2 g/cm3, and elastic modulus equal to 2.3 GPa) plastic by a 3D printer (Stratasys Inc., MN, USA) with resolution of 0.33 mm/layer. Three samples of each design were printed: hollow cylinders (4 cm in length, 1.9 cm in diameter, 0.2 cm in wall thickness), and similar cylinders with struts (0.15 cm in diameter, with a distance of 0.35 cm between struts) on the side, reinforcing struts were overlapped such that all cross-sections contained two struts inside the hollow tubes. Note that the samples tested in torsion contained larger sections with square cross-sections on the ends to be mounted in the device for twisting (the struts were printed all the way to the ends)

### 3.3. Torsion and ovalization testing

Torsion testing was performed using a custom built torsion testing device (Porter et al., 2015). The device was attached to the crossheads of an Instron materials testing machine (Instron 3367 Dual Column Testing Systems, Norwood, MA) and converts the applied linear displacement of the crosshead to a rotational displacement through a rack and pinion. The 3D printed prototypes were tested by applying a rotation to one end of the sample and recording the angle of twist as a function of applied load. All samples were tested until fracture.

Another set of 3D printed prototypes were tested in diametral compression to assess the effect of struts on ovalization. Tests were conducted on a universal testing machine equipped with 30 kN load cell (Instron 3367 Dual Column Testing Systems, Norwood, MA), using the compression mode between two platens with strain rate equal to $10^{-3}\,s^{-1}$. Load versus displacement curves were recorded for the tests. All samples were tested until fracture.

## 4. Results and discussion

### 4.1. Structural analysis

Fig. 5 shows a photograph of the turkey vulture humerus with regions indicated where cross-sectional photographs were taken (proximal end). Struts and ridges are observed in the cross-sections, which diminish in density away from the proximal end. The struts have elliptical cross-sections with major and minor axes ∼ 500 μm and 250 μm, respectively, as shown in the scanning electron micrograph. This ellipticity is apparently made to reduce the bending stress.

Fig. 6 depicts μ-CT cross-sectional images along the entire wing bone (humerus (a-f), ulna (g-l) and carpus (m-o)) of the condor. The bones decrease in diameter from the proximal to distal end. All bones show ovalization of their cross sections at the proximal and distal ends, with more circular shapes in the midsections. The trabecular bone at each end gradually changes to having strut-like components and then internal reinforcements disappear in the midsection.

Bending and torsion resistance have been suggested to be equally important in the humerus (Pennycuick, 1967; de Margerie et al., 2006; Biewerner and Dial, 1995). The humerus has exaggeratedly large proximal and distal ends compared with its midsection and with the other wing bones. The shapes at these ends are elongated in one direction, which appear to maximize *I* in the loading direction. The shape is also dictated by the placement of ligaments, tendons, and muscles. If the humerus is considered as a cantilever beam, loaded at the distal end, the bending moment decreases progressively from the proximal to distal end. The struts in Fig. 6c would be loaded in compression, thereby helping to prevent local buckling. The thickened and elliptical shape of the proximal end of the ulna (Fig. 6g,h) confirms that the bending and twisting moments in the humerus are transferred to the ulna as a bending moment (Pennycuick, 1967). Increased torsional resistance will be obtained by having circular cross-section, which is apparent in Fig. 6d, and can be further enhanced by adding material locally (ridges), which are observed in Fig. 6e. The ridges in these cross-sections appear as semi elliptical bumps on the bone interior, as they are flat against the inner bone wall. The ulna midsection appears more oval-shaped than circular. The carpus cross-section in Fig. 6m has an extension on the upper left, where the first digit or 'thumb' is extended. The carpus also has more oval-shaped midsections, indicating that it may be optimized for bending resistance.
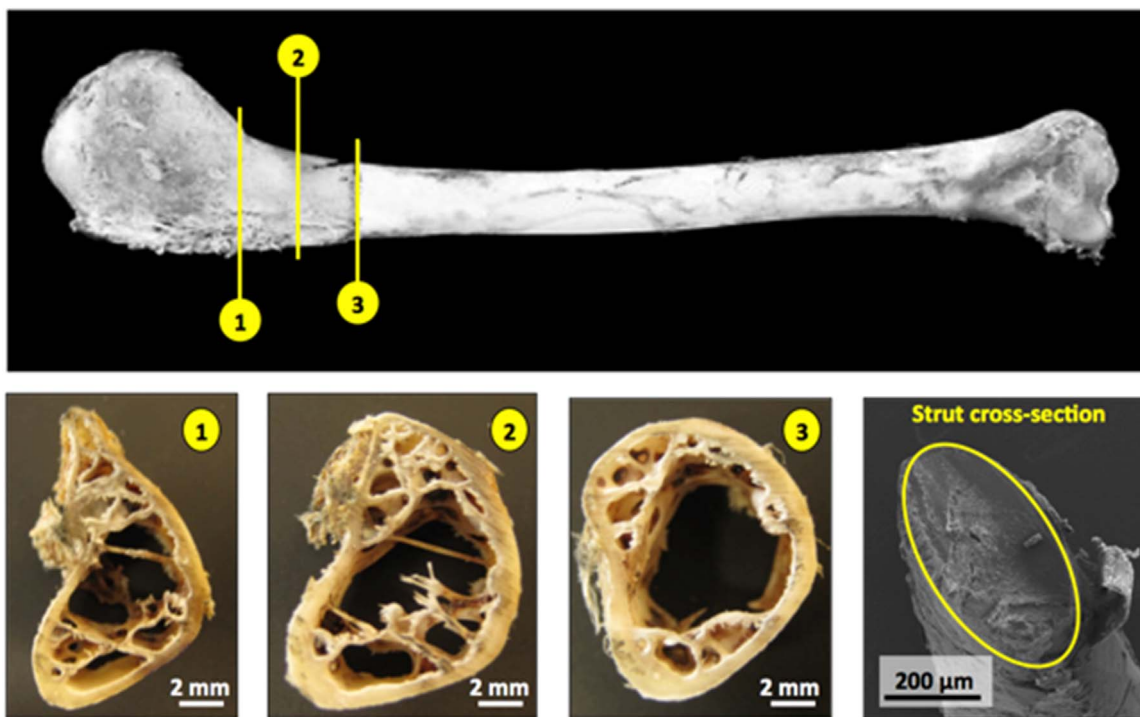
**Fig. 5.** Microscopic analysis of the turkey vulture humerus. Photograph showing cross-sections at the indicated position. A complex arrangement of struts are observed. A scanning electron micrograph of the elliptically-shaped strut.
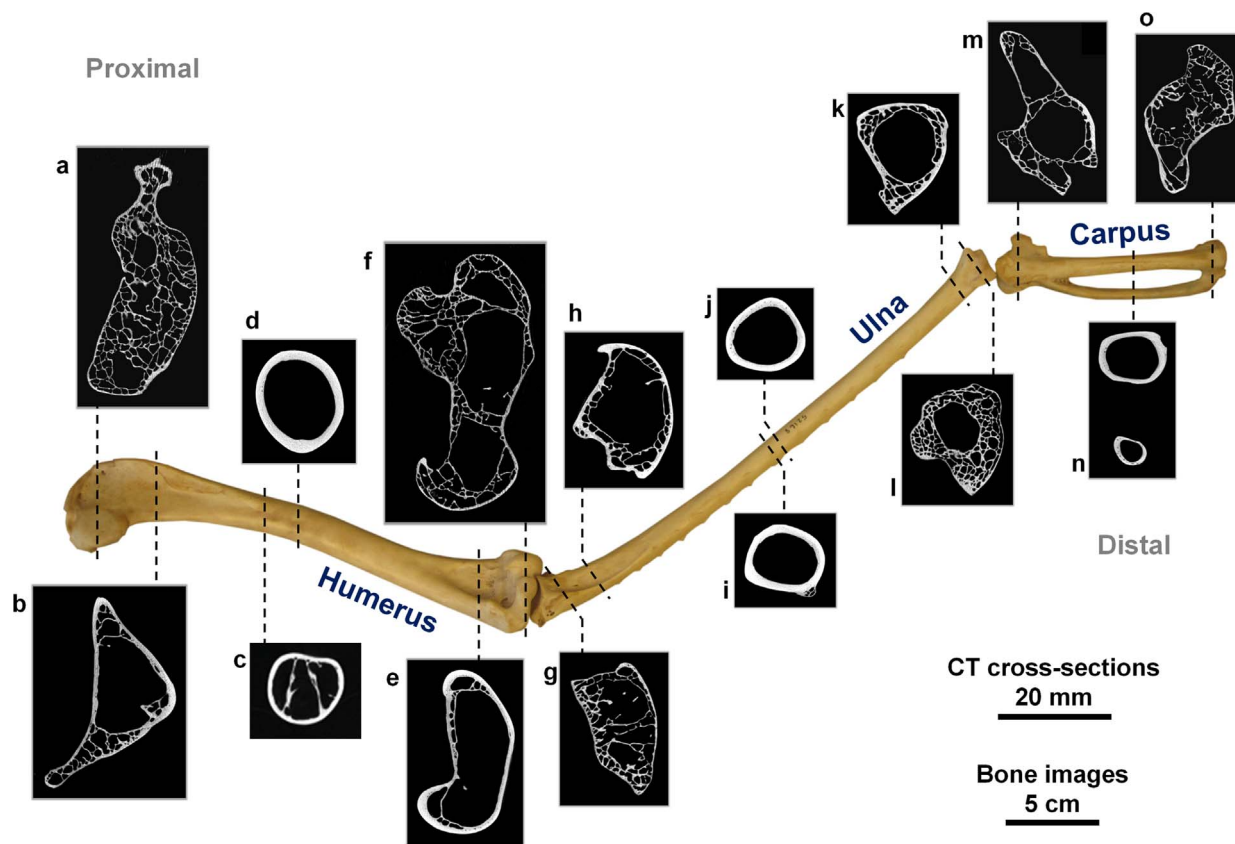


**Fig. 6.** Micro-computed tomography sectional along a condor wing. The proximal and distal ends of the humerus, ulna and carpus are ovalized, whereas the midsections are more circular. **(a)-(f)** Humerus, **(g)-(l)** ulna and **(m)-(o)** carpus.
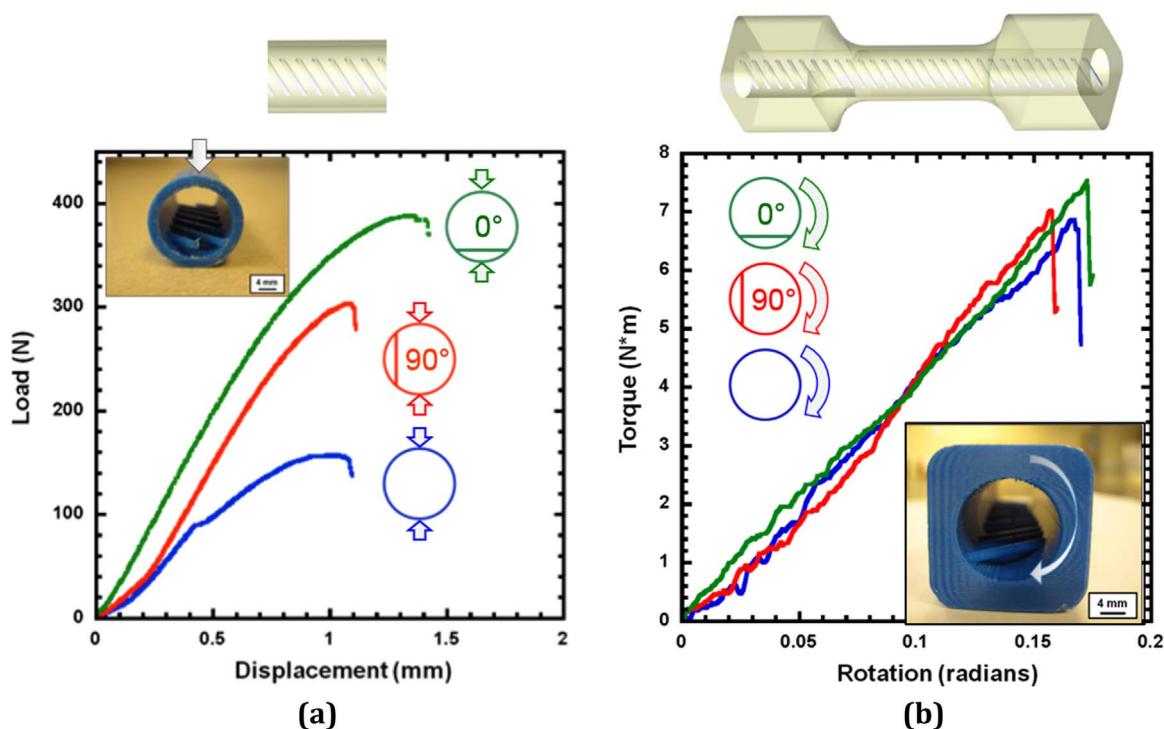
**Fig. 7.** Load frame test results on 3D-printed bone prototypes with no struts, and struts oriented at 0° (horizontal, green) and 90° (vertical, red). **(a)** Compressive load versus displacement curves. Both the 0° and 90° orientations allow for higher loads before failure. **(b)** Torque versus rotation angle, confirming that struts do not affect torsional resistance. Insets show photographs of the prototypes. SolidWorks models used to print the samples are added for visualization purposes. (For interpretation of the references to color in this figure legend, the reader is referred to the web version of this article.)

### 4.2. 3D printed prototypes: testing the hypothesis of reinforcing struts

Struts were placed inside cylindrical tubes simulating pneumatic bones to establish their effect on mechanical performance. The resistance to bending ovalization may be tested by a diametral compression test in which the distributed line forces were applied in the direction perpendicular to the cylinder axis, as shown in the insert of Fig. 7a. Particularly, Fig. 7a shows representative compressive load versus displacement curves on the 3D printed samples with no struts and struts oriented either horizontal (0°, perpendicular to the force direction) or vertical (90°, parallel to the force direction). The inset shows the samples tested, which were the ABS (blue) hollow cylinders with an array of parallel struts, a corresponding SolidWorks model was included for visualization purposes. The samples were compressed between parallel platens with the struts oriented as shown in the plot. All samples were tested until fracture. In diametral compression, both configurations with struts (0°, horizontal, in green and 90°, vertical, in red) show higher stiffness and strength compared to the hollow cylinder. The 0° orientation (in green) was optimal, with the highest modulus, strength and strain to failure. These samples withstood a 138% higher load and a 27% larger displacement compared to the hollow cylinder. In this configuration, the horizontal struts are under tension and resist ovalization of the cylinder.

For the 90° orientation, the struts are under compression and the samples have a 21% smaller load and a 20% smaller displacement than for the 0° orientation. This orientation of struts and applied load corresponds to the configuration of struts inside the bird wing bones loaded from the ventral side. These results demonstrate that struts appearing on the ventral side of bones increase the bending resistance during bird flight by decreasing ovalization.

The torsion samples (inset, Fig. 7b) were printed with square ends to fit into the torsion testing grips. The diameter of the torsion sample, the strut diameter and the orientation of the struts were the same as in the compression samples, a corresponding SolidWorks model was included for visualization purposes. Torsion test results show no significant

difference between the samples with and without struts, all three curves matched closely up to the fracture point. These results suggest that position and orientation of struts are optimized to resist bending, but not torsion. In the case of torsion, reinforcing ridges would be more effective; alternatively, the placement and orientation of ridges could be designed in a manner to counter the tensile forces created by torsion.

### 4.3. Analytical modeling: circular ring reinforced by vertical and horizontal struts

To gain a better understanding of the greater stiffening of the circular cylinder caused by the horizontal compared to the vertical struts, an analytical study of the stiffening and ovalization of a circular ring reinforced by the vertical or horizontal struts (Fig. 8a,c) was conducted. For simplicity we adopt a model of small elastic deformations. Both problems are four times statically indeterminate. For a vertically stiffened ring (90° orientation), by symmetry, it is sufficient to consider only the upper portion of the ring (Fig. 8b), while for the horizontally stiffened ring (0° orientation), it is sufficient to consider only the left portion of the ring (Fig. 8d). The unknown axial forces and bending moments ($X_1, X_2, X_3, X_4$) are determined by requiring that the corresponding displacements and slopes are equal to zero (due to the symmetry of the reinforced ring across its horizontal or vertical diameter). These conditions can be expressed in the standard canonical form (Gere and Timoshenko, 1990) as:

$$\delta_{i0} + \sum_{j=1}^{4} \delta_{ij} X_j = 0, i = 1, 2, 3, 4 \tag{5}$$

where $\delta_{ij} = \delta_{ji}$ are the Maxwell influence coefficients, equal for both vertical and horizontal struts. The coefficients $\delta_{i0}$ specify the displacements or the slopes at the considered points due to the applied force alone; they are different in the cases of the vertical vs. horizontal strut stiffening. All the coefficients ($\delta_{ij}$ and $\delta_{i0}$) can be calculated by the unit load construction of the structural mechanics analysis and are listed in
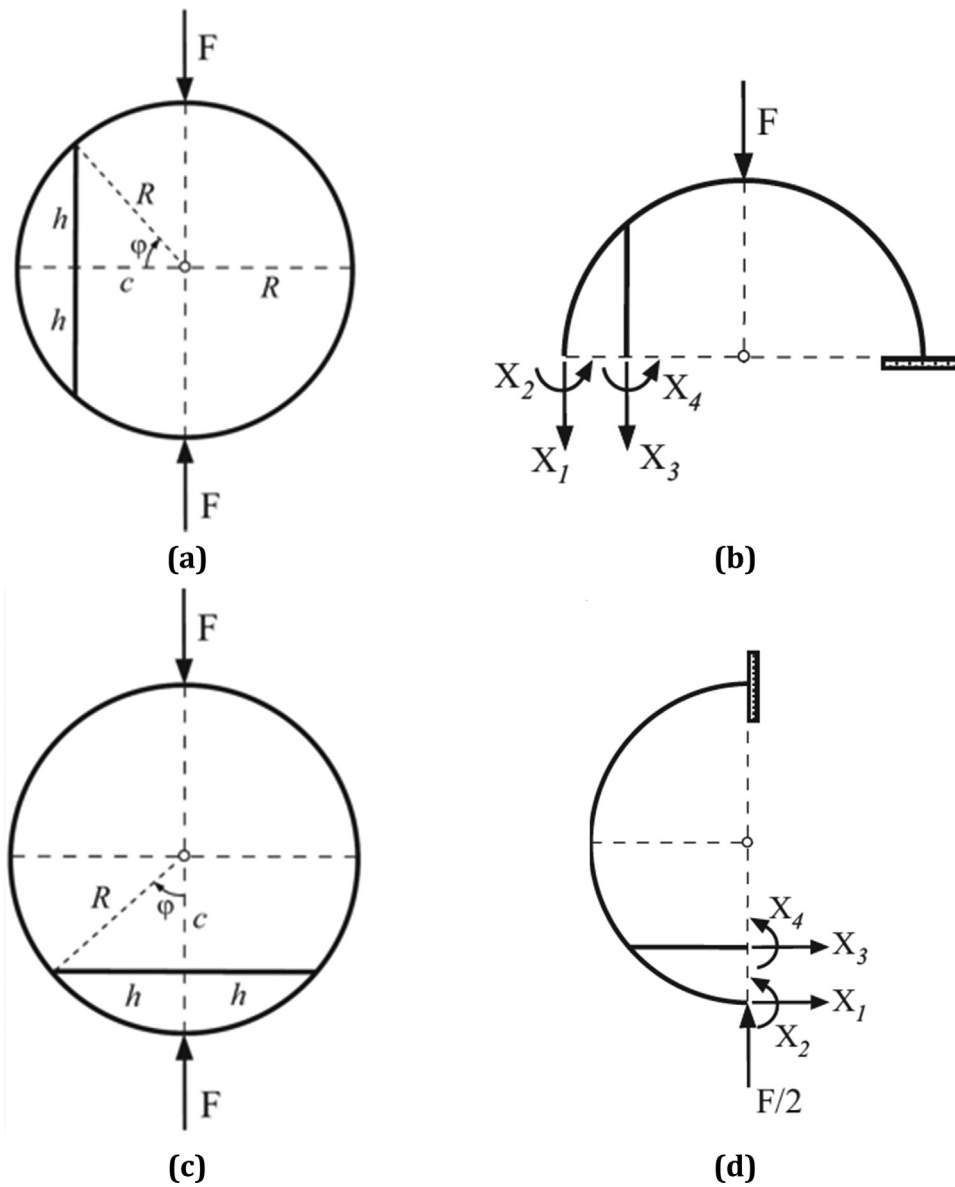
**Fig. 8.** Circular ring reinforced with a horizontal or vertical strut: **(a)** The circular ring of mid-radius $R$ under compressive forces $F$. The ring is reinforced by the vertical strut of length $2h$, located at the distance $c = \psi R$ from the center of the ring, so that $\cos\varphi = \psi$ and $\sin\varphi = h/R$. The bending stiffness of the strut is $E_s I_s = \alpha EI$, where $EI$ is the bending stiffness of the ring. **(b)** The upper-half of the ring with the indicated axial forces $(X_1, X_3)$ and bending moments $(X_2, X_4)$ in the cross-sections along the horizontal plane of symmetry. **(c)** The circular ring reinforced by the horizontal strut of length $2h$, located at the distance $c = \psi R$ from the center of the ring. **(d)** The left-half of the ring with the indicated axial forces $(X_1, X_3)$ and bending moments $(X_2, X_4)$ in the cross-sections along the vertical plane of symmetry.
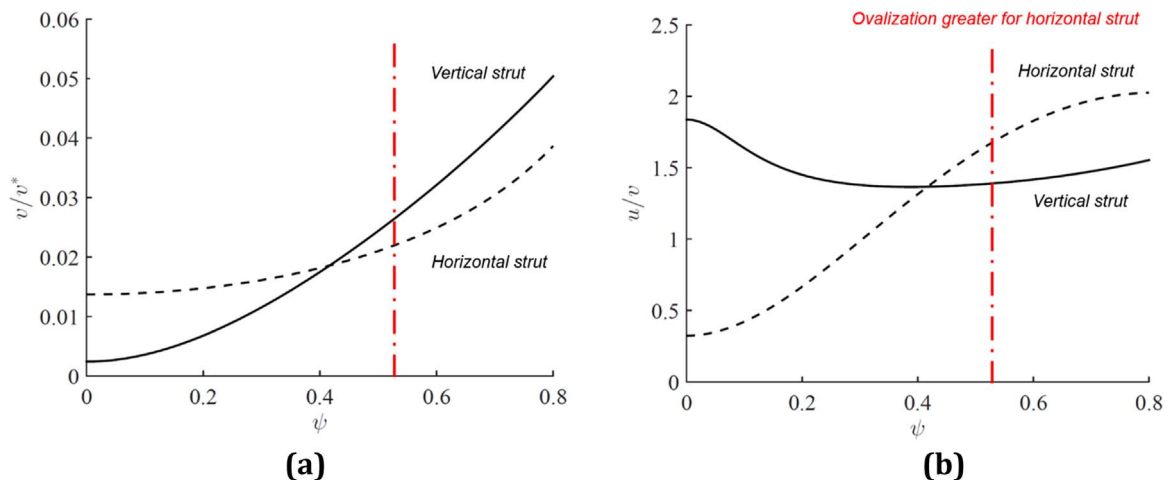


**Fig. 9.** Analysis of a circular ring reinforced with struts: **(a)** The shortening $v$ (scaled by $v^* = FR^3/EI$) of the vertical diameter of the ring vs. $\psi = c/R$ (position of the strut) for the vertical and horizontal strut. **(b)** The ovalization of the ring, given by the displacement ratio $u/v$, where $u$ is the elongation of the horizontal diameter of the ring due to applied vertical loads $F$. The red dashed line points out $\psi$ for the 3D printed prototypes.

the Appendix of this paper. The four linear algebraic equations (Eq. 5) for $X_i$'s were solved by the MATLAB software for each position of the reinforcing strut $c = \psi R$ (where $\psi = \cos\varphi$ (position of the strut), and $R$ is radius of the ring) in the range $0 \leq \psi \leq 0.8$. It is assumed that in the range of $\psi > 0.8$ the strut is sufficiently long (slender) for the elementary beam bending theory to apply. The vertical displacement ($v$) between the points of the load application (shortening of the vertical diameter of the ring) is calculated by superimposing the displacement contributions in the half-ring configurations shown in Fig. 8b,d from $F$ and $X_i$'s. This gives:

$$v = \sum_{i=1}^{4} X_i \delta_{i0} + \frac{FR^3\pi}{4EI} \, (vertical \, strut)$$

$$v = \sum_{i=1}^{4} X_i \delta_{i0} + \frac{FR^3\pi}{8EI} \, (horizontal \, strut) \tag{6}$$

Fig. 9a depicts the shortening of the vertical diameter of the ring vs. $\psi$ (position of the strut) for both, vertical and horizontal struts. For $\psi < 0.425$ (strut closer to the center of the ring), this shortening is greater in the case of the horizontal strut, but for $\psi > 0.425$ it is greater in the case of the vertically stiffened ring. As a consequence, for $\psi > 0.425$, a greater force is needed to produce a given vertical displacement (fattening of the ring) in the case of a stiffening of the ring by the horizontal strut. This explains the stiffening behavior observed in the experiments, reported in Fig. 7a, where we tested the 3D printed prototypes of the dimensions $R = 0.85$ cm and $c = 0.45$ cm, with the corresponding $\psi = 0.53 > 0.425$.

The horizontal displacement ($u$) between the end points of the horizontal diameter of the ring (specifying its lateral expansion due to applied vertical forces $F$) can also be calculated by using the unit load method of structural mechanics. By the Betti's reciprocal theorem of linear elasticity, the expansion of the ring along its horizontal diameter is equal for both stiffenings, by the vertical and horizontal strut, provided that $c$ (position of reinforcing strut) is the same in both cases. Thus, it suffices to determine $u$ in only one case of stiffening; this is done for the vertical strut in the Appendix of the paper. The results are used to calculate the ovalization of the ring, given by the displacement ratio $u/v$. This is shown in Fig. 9b. For $\psi < 0.425$, the ovalization is greater in the vertically stiffened ring, and for $\psi > 0.425$ in the horizontally stiffened ring.

## 5. Conclusions

The internal structures in the bones of the wings of a turkey vulture

and a condor were evaluated by micro-computed tomography and optical microscopy. The mechanical role of reinforcing struts was analyzed through torsion and diametral compression testing of 3D printed bone prototypes. The main findings are:

- Photographs of the humerus at different cross-sections near the proximal end showed a complicated network of struts, some spanning across the interior, and ridges, which are raised and elongated at various angles to the inner bone;
- The struts have elliptical cross-sections with major and minor axes $\sim 500\ \mu m$ and $250\ \mu m$, so shaped to resist compression and tension, thereby reinforcing the inner walls;
- Micro-computed tomography images of cross-sections along the entire wing bones showed progressively smaller diameters, with elliptically-shaped proximal and distal ends and more circular cross-sections in the midsections;
- Testing of 3D printed hollow cylinders with an array of struts placed off-axis to model the internal struts indicate that struts resist ovalization in diametral compression, while have no effect on torsional resistance;
- An elastic model of a circular ring reinforced by horizontal and vertical struts was used to explain the stiffening caused by differently oriented struts, in qualitative agreement with experimental results.

## Appendix

The Maxwell influence coefficients $\delta_{ij} = \delta_{ji}$ for the circular ring reinforced by either vertical or horizontal strut from Fig. 8a,c are

$$\delta_{11} = \frac{3}{2}\frac{R^3\pi}{EI},$$

$$\delta_{12} = \frac{R^2\pi}{EI},$$

$$\delta_{14} = (\pi - \varphi + \sin\varphi)\frac{R^2}{EI},$$

$$\delta_{13} = \left[\left(\psi + \frac{1}{2}\right)(\pi - \varphi) + (1 + \psi)\sin\varphi - \frac{1}{4}\sin 2\varphi\right]\frac{R^3}{EI},$$

$$\delta_{22} = \frac{R\pi}{EI}, \; \delta_{23} = [\psi(\pi - \varphi) + \sin\varphi]\frac{R^2}{EI}, \; \delta_{24} = (\pi - \varphi)\frac{R}{EI},$$

$$\delta_{33} = \left[\left(\psi + \frac{1}{2}\right)(\pi - \varphi) + 2\psi\sin\varphi - \frac{1}{4}\sin 2\varphi + \frac{\beta}{\alpha}\sin\varphi\right]\frac{R^3}{EI},$$

$$\delta_{34} = [\psi(\pi - \varphi) + \sin\varphi]\frac{R^2}{EI}, \; \delta_{44} = \left(\pi - \varphi + \frac{1}{\alpha}\sin\varphi\right)\frac{R}{EI}.$$

The location of the strut is specified by $c = \psi R$ ($\psi = \cos\varphi$), where $0 \leq \psi \leq 1$, although the upper bound of $\psi$ is less than one (say $\sim 0.8$) in order that the strut is long enough to be treated by the beam theory. In terms of the angle $\varphi$ shown in Fig. 8a,c, $\psi = \cos\varphi$ and $h = R\sin\varphi$, where $R$ is the mid-radius of the thin ring and $2h$ is the length of the strut. The parameter $\alpha$ is the ratio of the bending stiffness of the strut $E_s I_s$ and the ring, $\alpha = E_s I_s$

/EI, while the parameter $\beta$ is defined such that $I_s/A_s = \beta R^2$, where $I_s$ and $A_s$ are the moment of inertia and the area of the cross-section of the strut. In calculations reported in Section 3.3, we selected $\alpha = 1$ and $\beta = 2.5 \times 10^{-3}$. This value of $\beta$ corresponds to circular cross-section of the strut whose radius is 1/10 of the radius of the ring.

The coefficients $\delta_{i0}$, in the case of the reinforcement by the vertical strut (Fig. 8b), are

$$\delta_{10} = \left(1 + \frac{\pi}{4}\right)\frac{FR^3}{EI},$$

$$\delta_{20} = \delta_{40} = \frac{FR^2}{EI},$$

$$\delta_{30} = \left(\psi + \frac{\pi}{4}\right)\frac{FR^3}{EI}.$$

If the ring is reinforced by the horizontal strut (Fig. 8d), the coefficients $\delta_{i0}$ are

$$\delta_{10} = \frac{FR^3}{EI},$$

$$\delta_{20} = \frac{FR^2}{EI},$$

$$\delta_{40} = \frac{1}{2}(1 + cos\varphi)\frac{FR^2}{EI},$$

$$\delta_{30} = \frac{1}{2}\left[\psi(1 + cos\varphi) + \frac{1}{2}sin^2\varphi\right]\frac{FR^3}{EI}.$$

The horizontal displacement, i.e., the increase of the ring's length along its horizontal diameter, can be determined by summing the integral contributions along the ring from the products of the moment $M_k$ due to loading shown in Fig. A1a and the moment due to the unit load shown in Fig. A1b,

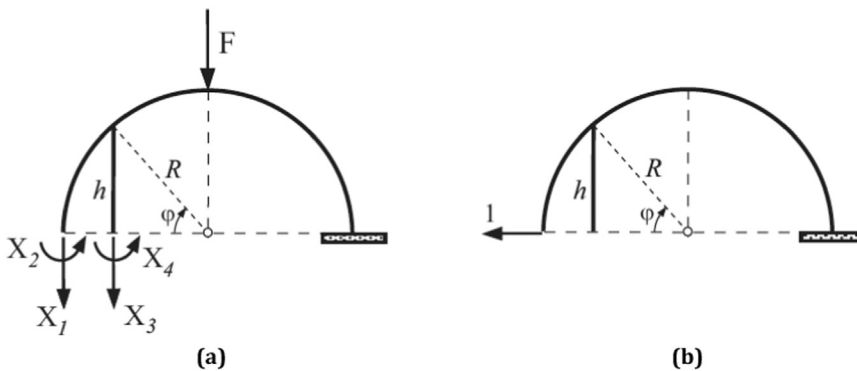$$u = \sum_k \int \frac{M_k \overline{M_k}}{EI} dl.$$



**Fig. A1.** (a) The upper-half of the circular ring reinforced by the vertical strut, with the indicated axial forces $(X_1, X_3)$ and bending moments $(X_2, X_4)$ in the cross-sections along the horizontal plane of symmetry. (b) The unit load in the direction of the horizontal displacement $u$.

(a)　　　　　　　　　　　　　　　　　　(b)

It follows that

$$u = -(A_1 + A_2 + A_3)\frac{R^2}{EI},$$

where, upon integration,

$$A_1 = X_1 R\left(1 - cos\varphi - \frac{1}{2}sin^2\varphi\right) + X_2(1 - cos\varphi),$$

$$A_2 = X_1 R\left(cos\varphi - \frac{1}{2}cos^2\varphi\right) + X_2 cos\varphi + X_3 R\left(\psi cos\varphi - \frac{1}{2}cos^2\varphi\right) + X_4 cos\varphi,$$

$$A_3 = \frac{3}{2}X_1 R + X_2 cos\varphi + X_3 R\left(\frac{1}{2} + \psi\right) + X_4 + \frac{1}{2}FR.$$

## References

Biewerner, A.A., Dial, K.P., 1995. In vivo strain in the humerus of pigeons (*Columbia livia*) during flight. J. Morphol. 225, 61–75.

Brazier, L.G., 1927. On the flexure of thin cylindrical shells and other "thin" sections. Proc. R. Soc. Lond. A 116, 104–114.

Brodkorb, P., 1955. Number of feathers and weights of various systems in a bald eagle. Wilson Bull. 67, 142.

Bruderer, B., Dieter, P., Boldt, A., Liechti, F., 2010. Wing-beat characteristics of birds recorded with tracking radar and cine camera. Ibis 152, 272–291.

Casinos, A., Cubo, J., 2001. Avian long bones, flight and bipedalism. Comp. Biochem. Physiol. Part A 131, 159–167.

Cubo, J., Casinos, A., 2000. Incidence and mechanical significance of pneumatization in the long bones of birds. Zool. J. Linn. Soc. 130, 499–510.

Currey, J.D., Alexander, R.M., 1985. The thickness of the walls of tubular bones. (453-388) J. Zool. Soc. Lond. 206 (453-388).

Currey, J.D., Zioupos, P., Davies, P., Casinos, A., 2001. Mechanical properties of nacre and highly mineralized bone. Proc. R. Soc. B 268, 107–111.

Davis, P.G., 1998. The bioerosion of bird bones. Int. J. Osteoarcheol. 7, 388–401.

Dumont, E.R., 2010. Bone density and the lightweight skeletons of birds. Proc. R. Soc. B 277, 2193–2198.

Etnier, S.A., 2003. Twisting and bending of biological beams: distribution of biological beams in a stiffness mechanospace. Biol. Bull. 205, 36–46.

Gere, J.M., Timoshenko, S.P., 1990. Mechanics of Materials. PWS-KENT Publishing Company, Boston.

Gill, F.B., 2007. Ornithology. (3rd. ed.) W.H. Freeman & Company, New York, NY.

Kiang J.H., 2013. Avian Wing Bones. M.S. Thesis: UC San Diego, La Jolla, CA.

Lubarda, V.A., 2009. On the torsion constant of multicell profiles and its maximization with respect to spar position. Thin-Walled Struct. 47, 789–806.

de Margerie, E., Sanchez, S., Cubo, J., Castanet, J., 2006. Torsional resistance as a principal component of the structural design of long bones: Comparative multivariate evidence in birds. Anat. Rec. A 282, 49–66.

Niklas, K.J., 1992. Plant Biomechanics, An Engineering Approach to Plant Form and Function. University of Chicago Press, Chicago, IL.

Novitskaya, E., Castro-Ceseña, A.B., Chen, P.-Y., Lee, S., Hirata, G., Lubarda, V.A., McKittrick, J., 2011. Anisotropy in the compressive mechanical properties of bovine cortical bone: mineral and protein constituents compared with untreated bone. Acta Biomater. 7, 3170–3177.

Novitskaya, E., Ribero Vairo, M.S., Kiang, J., Meyers, M.A., McKittrick, J., 2014. Reinforcing structures in avian wing bones. In: Narayan, R., McKittrick, J. (Eds.), 10th Pacific Rim Conference on Ceramic and Glass Technology. Wiley, San Diego, CA, pp. 47–56.

O'Connor, P.M., Claessens, L.P.A.M., 2005. Basic avian pulmonary design and flow-through ventilation in non-avian theropod dinosaurs. Nature 436, 253–256.

Pauwells, F., 1980. Biomechanics of the Locomotor Apparatus. Springer, Berlin.

Pennycuick, C.J., 1967. The strength of the pigeon's wing bones in relation to their function,". J. Exp. Biol. 26, 219–233.

Pennycuick, C.J., 2008. Modelling the Flying Bird. Elseview Academic Press, San Diego, CA.

Pilkey, W.D., 2003. Analysis and Design of Elastic Beams: Computational Methods. John Wiley and Sons, New York, N.Y.

Porter, M.M., Meraz, L., Calderon, A., Choi, H., Chouhan, A., Wang, L., Meyers, M.A., McKittrick, J., 2015. Torsional properties of helix-reinforced composites fabricated by magnetic freeze casting. Compos. Struct. 119, 174–184.

Proctor, N.S., Lynch, P.J., 1993. Manual of Ornithology: Avian Structure and Function. Yale University Press, New Haven, CT.

Reilly, D.T., Burstein, A.H., 1975. The elastic and ultimate properties of compact bone tissue. J. Biomech. 8, 393–405.

Ruff, C., Holt, B., Trinkaus, E., 2006. Who's afraid of the big bad Wolff? "Wolff's Law" and bone functional adaption. Am. J. Phys. Anthropol. 129, 484–498.

Silva, M.A., Brown, J.H., Downing, J.A., 1997. Differences in population density and energy use between birds and mammals: a macroecological perspective. J. Anim. Ecol. 66, 327–340.

Spatz, H.-C., O'Leary, E.J., Vincent, J.F.V., 1996. Young's moduli and shear moduli in cortical bone. Proc. R. Soc. Lond. B 263, 287–294.

Swartz, S.M., Bennett, M.B., Carrier, D.R., 1992. Wing bone stresses in free flying bats and the evolution of skeletal design for flight. Nature 359, 726–729.

Vogel, S., 1992. Twist-to-bend ratios and cross0sectional shapes of petioles and stems. J. Exp. Biol. 43, 1527–1532.

Wolfson, A., 1955. Recent Studies in Avian Biology. University of Illinois Press, Urbana, IL.

Zioupos, P., Currey, J.D., Casinos, A., 2000. Exploring the effects of hypermineralisation in bone tissue by using an extreme biological example. Connect. Tissue Res. 41, 229–248.